Control Engineering Practice 145 (2024) 105856

Contents lists available at ScienceDirect

Control Engineering Practice

journal homepage: www.elsevier.com/locate/conengprac

Efficient computation of robust, safe, fast charging protocols for lithium-ion batteries

Giacomo Galuppini, Marc D. Berliner, Huada Lian, Debbie Zhuang, Martin Z. Bazant, Richard D. Braatz *

Massachusetts Institute of Technology, Cambridge, MA 02139, USA

ARTICLE INFO

Keywords:
Lithium-ion batteries
Lithium iron phosphate
Multiphase porous electrode theory
Fast charging
Charging protocols
Stochastic optimal control

ABSTRACT

The design of fast charging protocols is fundamental to improving the performance and lifetime of lithium-ion batteries. It is well-known that charging operations consistently performed at very high current will negatively impact operational safety and battery lifetime, although a quantitative understanding of these relationships remains lacking. The protocol design problem is typically formulated as a model-based dynamic optimization, where safety of operations can be encoded by constraining relevant battery states. However, all models are affected by uncertainty, which in turn propagates to state predictions. In this case, charging protocols based on *nominal* predictions may not satisfy the operating constraints. To overcome this issue, this work proposes a stochastic optimal control approach for the efficient computation of safe, fast charging protocols, able to explicitly account for parametric uncertainties affecting the battery model and guarantee probabilistically robust constraint satisfaction. Given a description of uncertainty affecting model parameters, linearized sensitivity analysis is exploited to propagate uncertainty to the battery states, and suitable backoff values for safety constraints are computed for each time instant. The effectiveness of the methodology is demonstrated in silico, by computing five different protocols, with a detailed Multiphase Porous Electrode Theory-based model of commercially available lithium-iron-phosphate batteries.

1. Introduction

Lithium-ion batteries have become ubiquitous in electrochemical energy storage and are having a huge impact on modern technology. However, further spread of this technology is still limited by the charging time of the battery. While charging at high C-rates is technically possible, it is well-known that charging operations consistently performed at very high current can pose safety risks and severely shorten battery lifetime (Ahmed et al., 2017; Tarascon & Armand, 2011). These effects can be attributed to increased growth rate of the solid-electrolyte interface (SEI) layer, higher temperatures, higher mechanical stresses, and increased lithium plating, Anseán, Dubarry, Devie, Liaw, García, Viera, and González (2016), Anseán et al. (2013), Mathieu, Briat, Gyan, and Vinassa (2021), Tomaszewska et al. (2019), Xu, Wang, Reichman, and Wang (2018) and Xu, Wang, Zhang, and Zhao (2021). For these reasons, the design of fast charging protocols for lithium-ion batteries is currently an area of high research activity (Chaturvedi, Klein, Christensen, Ahmed, & Kojic, 2010; Kollmeyer, Hackl, & Emadi, 2017; Mohtat, Pannala, Sulzer, Siegel, & Stefanopoulou, 2021; Notten, Bert, & Van Beek, 2005; Pozzi, Moura, & Toti, 2023).

The design of fast charging protocols is typically addressed in the literature using optimal (Berliner, Jiang, Cogswell, Bazant, & Braatz, 2022a; Galuppini, Berliner, Lian, et al., 2023; Nambisan, Saha, & Khanra, 2021; Xu, Wang, Zhao, & Wang, 2019) or Model Predictive Control (MPC) techniques (Kolluri, Aduru, Pathak, Braatz, & Subramanian, 2020; Perez, Dey, Hu, & Moura, 2017; Pozzi & Raimondo, 2022; Pozzi, Torchio, Braatz, & Raimondo, 2020; Pozzi & Toti, 2022; Zou, Manzie, & Nešić, 2018). In both cases, the design problem is formulated as a dynamic optimization, where cost function and constraints model the conflicting requirements on speed and safety of charging operations. Both optimal control and MPC heavily rely on the knowledge of a dynamic model of the battery, which can range from simple equivalent-circuit models to Porous Electrode Theory (PET) or Multiphase Porous Electrode Theory (MPET) models. While equivalent circuit or reduced-order models are typically characterized by very low computational complexity, they do not capture all the relevant battery dynamics, such as thermodynamic effects and degradation mechanisms (Hu, Li, & Peng, 2012; Krewer et al., 2018; Speltino, Di Domenico, Fiengo, & Stefanopoulou, 2009; Zou, Manzie, & Anwar,

* Corresponding author.
E-mail address: braatz@mit.edu (R.D. Braatz).

https://doi.org/10.1016/j.conengprac.2024.105856
Received 11 August 2023; Received in revised form 24 November 2023; Accepted 14 January 2024
Available online 18 January 2024

2014). On the other hand, PET and MPET models can provide much more physical insight and predictive capability, at the price of much higher computational complexity, as they typically consist of a (possibly huge) set of Differential–Algebraic Equations (DAEs) (Berliner, Cogswell, Bazant, & Braatz, 2021; Newman, 1998; Smith & Bazant, 2017; Torchio, Magni, Gopaluni, Braatz, & Raimondo, 2016).

Regardless of their complexity, all models are affected by uncertainty in their predictions. While closed-loop control schemes such as MPC provide some inherent form of robustness with respect to model uncertainties (Rawlings, Mayne, & Diehl, 2017), it is necessary to explicitly account for plant-model mismatch when dealing with optimal open-loop control (Galuppini, Berliner, Lian, et al., 2023). A common approach in optimal control is based on the implementation of tightened constraints, which are *backed off* from their original values to account for model uncertainties (Bryson & Ho, 2018; Srinivasan, Palanki, & Bonvin, 2003). Additionally, when dealing with parametric models, uncertainty affecting model parameters can be characterized and then propagated to model predictions (Caracotsios & Stewart, 1995; Nagy & Braatz, 2007). An optimal control problem can then be formulated to guarantee robust or probabilistically robust constraint satisfaction, as well as robust performances, by exploiting constraint backoff values based on the uncertainty description.

An efficient approach for the computation of safe, fast charging protocols via optimal control and (M)PET models was recently proposed and demonstrated (Berliner et al., 2022a; Galuppini, Berliner, Lian, et al., 2023). The main goal of this work is to combine this efficient optimal control approach with uncertainty propagation techniques (Caracotsios & Stewart, 1995; Galán, Feehery, & Barton, 1999; Nagy & Braatz, 2004, 2007), and propose a stochastic optimal control algorithm for the efficient computation of safe, fast charging protocols in the presence of model uncertainties. Given a stochastic description of uncertainty affecting model parameters, a stochastic description of uncertainty affecting the evolution of the battery states is obtained at each time instant, by means of linearized sensitivity analysis techniques (Caracotsios & Stewart, 1995). Based on these results, suitable backoff values for safety constraints are introduced in the optimal control problem, and their values updated at each time instant to guarantee stochastic constraint satisfaction with minimum backoff. Compared to standard approaches for the computation of fast charging protocols, the methodology proposed in this paper reduces the required computational burden (from that of a stochastic optimization, to that of a few simulations), does not require any *a priori* parameterization of the current profile, and leverages the adaptive time-stepping algorithms in DAE solvers to handle stiffness.

In order to illustrate the proposed methodology for state-of-the-art applications, we consider the general case of MPET battery models and investigate fast charging protocols for one of the most popular battery chemistries. In particular, we model A123 System's *APR18650M1A* batteries with graphite anodes and lithium iron phosphate (LFP) cathodes (*A123 Systems official website*, 2023), each consisting of multiphase porous materials, which require the MPET framework for consistent modeling based on nonequilibrium thermodynamics (Ferguson & Bazant, 2014; Smith & Bazant, 2017). Specifically, several protocols involving safety constraints on power, lithium-plating overpotential, temperature, and electrolyte and solid-phase concentrations are computed in the presence of uncertainty affecting several model parameters and the results thoroughly discussed to underline advantages, limitations, and possible improvements of the approach.

The paper is organized as follows: Section 2.1 provides details on MPET with comparison to standard PET; Section 2.2 briefly discusses MPET as a set of DAEs; Section 2.3 discusses the methodology adopted for uncertainty propagation; Section 2.4 summarizes the general battery operating mode framework; Section 2.5 describes the approach for computing safe, fast charging protocols. Details of the specific case study investigated in this work are given in Section 3. A set of protocols are computed and analyzed in Section 4, while Section 5 further discusses the design methodology. Finally, Section 6 concludes this work by summarizing its findings.

2. Methods

2.1. Porous electrode theory for multiphase lithium-ion batteries

Lithium-ion batteries consist of two electrodes and a separator between them. Electrodes and separator are characterized by a porous structure. The porous electrodes include several intercalating phases (electrolyte and active material, binder, and conductive additive). During charge and discharge operations, lithium undergoes several transport and electrochemical reaction processes, and moves from the active material of the one electrode to the other. This complex dynamic behavior can be modeled using porous electrode theory (PET) (Newman & Tiedemann, 1975), which has been widely validated, and is currently available in a number of software implementations (e.g., Berliner, Cogswell, et al., 2021; Fang, Kwon, & Wang, 2010; Newman, 1998; Torchio et al., 2016). In PET, the transport of lithium ions is described by Stefan–Maxwell concentrated solution theory, and solid active material and electrolyte in each electrode are coupled by Butler–Volmer (BV) kinetics. Finally, solid-phase transport is modeled as Fickian diffusion.

In recent years, multiphase porous electrode theory (MPET) has been developed with a more detailed thermodynamics model enabling the modeling of multiphase materials which occur in some important classes of lithium-ion batteries (Ferguson & Bazant, 2012, 2014; Smith & Bazant, 2017). In standard PET, *empirical* models of the thermodynamics of the active materials are obtained by fitting Open Circuit Voltage (OCV) versus State Of Charge (SOC) measurements. As a result, the thermodynamics of active materials characterized by multiple stable phases cannot be described. On the contrary, MPET models the free energy functional of multiphase materials, and electrochemical activities, overpotentials, and reaction rates are then defined consistently with the free energy. With MPET. The description of the solid-state dynamics is also improved by simulating multiple, interacting particles both along and in parallel to the main direction of current flow. As for particle size and conductance values, lognormal distributions are used to draw suitable values. MPET also allows for several particle shapes and active particle reaction models, which can be assigned separately for particles in the two electrodes (Bazant, 2013; Smith & Bazant, 2017). Several alternatives to the empirical Butler–Volmer model of reaction kinetics are available in MPET. Alternative reaction kinetics are based on Marcus theory of electron transfer (Chidsey, 1991; Marcus, 1956, 1957) applied to ion intercalation in solids (Bai & Bazant, 2014) and its generalization for coupled ion-electron transfer (Fraggedakis et al., 2021). Finally, the dilute model or the full Stefan–Maxwell concentrated solution theory (Smith & Bazant, 2017) can be used to describe the electrolyte. MPET modeling of lithium-plating phenomena is also improved by incorporating a nucleation barrier into the lithium-plating reaction (Baker & Verbrugge, 2020; Gao et al., 2021; Pei, Zheng, Shi, Li, & Cui, 2017). Finally, nonisothermal effects are also included, based on well-established modeling methodologies (Newman & Thomas-Alyea, 2012; Torchio et al., 2016).

The simulations in this work are based on an extension of a freely available Python implementation of MPET (Smith & Bazant, 2017), which is discussed in detail elsewhere (Galuppini, Berliner, Lian, et al., 2023).

2.2. Differential algebraic equations

When expressed in the general *fully implicit* form, a set of DAEs can be written as

$$F(t, \dot{x}(t), x(t), u(t), \theta) = 0 \tag{1}$$

where t is time, $x(t)$ is the vector of states, $\dot{x}(t)$ is its time derivative, $u(t)$ is the vector of inputs, and θ is the vector of parameters. Solvers (e.g., Andersson, Gillis, Horn, Rawlings, & Diehl, 2019; Hindmarsh et al., 2005) are available for simulating such DAEs, to compute the

time derivative of differential terms $\dot{x}(\bar{t})$, and the value of algebraic terms $x(\bar{t})$ at each time instant $\bar{t}$.

MPET models are formulated as systems of DAEs: differential states include electrolyte concentration c_e, solid particle concentrations c_s, and temperature T, while algebraic states include ionic fluxes j, electrolyte potential Φ_e, and solid particle potentials Φ_s. The MPET implementation adopted in this work (Smith & Bazant, 2017) uses the Python package *DAE Tools* (Nikolić, 2016) for the specification of DAEs, and the *SUNDIALS* suite (Hindmarsh et al., 2005) as the DAE solver.

2.3. Distributional uncertainty and uncertainty propagation

To simplify the presentation of the sensitivity analysis, we reformulate (1) as an explicit DAE:

$$E\dot{\xi}(t) = f(x(t), u(t), \theta). \tag{2}$$

where E is a matrix derived by algebraic manipulation. We define θ^* as the nominal model parameter vector, and $\delta\theta$ as a perturbation about θ^*. Then, the model parameter vector can be written as

$$\theta = \theta^* + \delta\theta. \tag{3}$$

We choose $\delta\theta$ to be a Gaussian random variable, $\delta\theta \sim \mathcal{N}(0, \mathbf{V}_\theta)$, which implies that $\theta \sim \mathcal{N}(\theta^*, \mathbf{V}_\theta)$. This uncertainty in the model parameters can be equivalently represented in terms of a confidence hyperellipsoid,

$$\epsilon_\theta = \left\{ \theta : (\theta - \theta^*)^\top \mathbf{V}_\theta^{-1} (\theta - \theta^*) \le \chi^2_{N_\theta}(\alpha) \right\}, \tag{4}$$

parameterized by α, where $\chi^2_{N_\theta}$ is the chi-squared distribution with N_θ degrees of freedom, N_θ is the number of parameters, and α is the desired level of significance.

Using a similar notation as in (3), we define $\xi^*(t)$ as the nominal state evolution, and $\delta\xi(t)$ as its perturbation due to the effect of $\delta\theta$, that is, $\xi(t) = \xi^*(t) + \delta\xi(t)$. We expand $\delta\xi(t)$ as a power series leads to

$$\delta\xi(t) = L(t)\delta\theta + \tfrac{1}{2}\delta\theta^\top \mathbf{M}(t)\delta\theta + \cdots \tag{5}$$

where

$$L(t) = \left.\frac{\partial \xi(t)}{\partial \theta}\right|_{\theta=\theta^*}; \quad \mathbf{M}(t) = \left.\frac{\partial^2 \xi(t)}{\partial \theta^2}\right|_{\theta=\theta^*}. \tag{6}$$

The elements of $L(t)$ and $\mathbf{M}(t)$ can be computed using finite differences or by integrating the model's DAEs augmented with the sensitivity equations (Caracotsios & Stewart, 1995):

$$E\dot{L}(t) = \mathbf{J}_x L(t) + \mathbf{J}_\theta \tag{7}$$

where

$$\mathbf{J}_x = \frac{\partial f(x(t), u(t), \theta)}{\partial \xi}; \quad \mathbf{J}_\theta = \frac{\partial f(x(t), u(t), \theta)}{\partial \theta}. \tag{8}$$

Due to the uncertainty in the model parameters, ξ is a random variable. Typically the uncertainty in the state, $\delta\xi(t)$, can be accurately related to the uncertainty in the model parameters, $\delta\theta$, by using only the first-order term in (5), which results in Blitzstein and Hwang (2015)

$$\xi(t) \sim \mathcal{N}(\xi^*(t), \mathbf{V}_\xi(t)), \tag{9}$$

$$\mathbf{V}_\xi(t) = L(t)^\top \mathbf{V}_\theta\, L(t). \tag{10}$$

Since the nominal value for ξ^* and the vector of sensitivities L are functions of time, the state distribution is also a function of time. The first-order approximation also allows the derivation of an analytical expression for the (probabilistic) worst-case state $\xi^{\text{w.c.}}(t)$ corresponding to the significance level α (Ma, Chung, & Braatz, 1999).

At each time instant t, the problem to be solved is

$$\max_{\theta \in \epsilon_\theta} (\delta\xi)^\top \mathbf{W} (\delta\xi) \tag{11}$$

$$= \max_{\theta \in \epsilon_\theta} \delta\theta^\top L^\top \mathbf{W} L \delta\theta \tag{12}$$

where $\mathbf{W}$ is a positive-definite weighting matrix (in this work, it is chosen as the identity matrix). To simplify the computations, we define

$$\beta = \chi^{-1}_{N_\theta}(\alpha) \mathbf{V}_\theta^{-1/2} \delta\theta. \tag{13}$$

Substituting (13) into (12) leads to

$$\max_{\beta^\top\beta \le 1} \chi^2_{N_\theta}(\alpha)\, \beta^\top \left(\mathbf{V}_\theta^{1/2}\right)^\top L^\top \mathbf{W} L \mathbf{V}_\theta^{1/2} \beta, \tag{14}$$

which has the solution (Golub & Van Loan, 1996)

$$\beta^{\text{w.c.}} = \pm \nu_1 \tag{15}$$

where

$$\mathbf{W}^{1/2} L \mathbf{V}_\theta^{1/2} = \mathbf{U}\mathbf{\Sigma}\mathbf{Z}^\top \tag{16}$$

is the singular value decomposition, and ν_1 is the leftmost column of $\mathbf{Z}$. A worst-case parameter is

$$\delta\theta^{\text{w.c.}} = \pm\, \chi_{N_\theta}(\alpha) \mathbf{V}_\theta^{1/2} \nu_1, \tag{17}$$

resulting in a worst-case uncertainty in the state evolution of

$$\delta\xi^{\text{w.c.}} = \pm\, \chi_{N_\theta}(\alpha) L \mathbf{V}_\theta^{1/2} \nu_1 \tag{18}$$

with + or − depending on the presence of upper or lower bounds on each state. As an example, assuming a significance level $\alpha = 0.05$, at each time instant, the value of the state $\xi(t)$ is expected to fall in the interval $[\xi^* - \delta\xi^{\text{w.c.}}; \xi^* + \delta\xi^{\text{w.c.}}]$ with probability 95%, which represents the worst-case scenario. This expression is used in the next section to specify backoffs in the optimal charging problems.

Remark. The choice of a first-order series expansion in the uncertainty propagation is motivated by a preliminary investigation for PET models (Pedret Sagnier, 2022). By comparing to the second-order series expansion in (5), and to Monte Carlo sampling of the full nonlinear PET model, the work showed that the first-order series expansion is highly accurate for optimal charging calculations. Moreover, the choice of a first-order series expansion is also motivated by efficiency. The first-order expansion can be obtained with a central finite difference approximation, which requires only a limited number of simulations. The simulations can be performed in parallel, to further reduce the computation time.

Remark. For parameter values that span several orders of magnitude, a standard finite difference approach for the computation of parameter sensitivities may lead to inaccurate results, as the differentiation step may become close to machine precision (Caracotsios & Stewart, 1995; Nagy & Braatz, 2007). To overcome this issue, it is advisable to rely on the computation of a *logarithmic sensitivity* of the form:

$$L_{\log}(t) = \left.\frac{\partial \xi(t)}{\partial \log_{10} \theta}\right|_{\theta=\theta^*}, \tag{19}$$

which can be then related to the standard sensitivity (6) by

$$L(t) = \frac{L_{\log}(t)}{\log_{10} \theta^*}. \tag{20}$$

2.4. Worst-case battery operating modes

PET and MPET software implementations typically offer constant voltage, current, and power operation modes (Berliner, Cogswell, et al., 2021; Newman, 1998; Torchio et al., 2016). A generalization of the battery operating mode concept to consider arbitrary states involved in the battery dynamics was recently proposed in Berliner et al. (2022a). In this framework, any state of interest can be forced to follow a user-specified time evolution, by including current among the DAE states and appending a specific constraint involving the state of interest to the set of DAEs. In case of parameter uncertainty, the time evolution of the states may be also uncertain. Given a description of parametric

uncertainty, the propagation approach discussed in the previous section can then be introduced in the algorithm to force the worst-case time evolution of any state of interest, as described in the reminder of this section.

2.4.1. Computation of nominal battery operating modes

Consider a generic *algebraic* state of interest ξ, and the corresponding ξ operating mode. Let $\overline{\xi}(t, \dot{x}(t), x(t))$ be the desired time evolution for ξ. The current $I(t, \dot{x}(t), x(t))$ is then treated as a state of the DAEs, rather than an input, and its time evolution constrained by the residual:

$$I(t, \dot{x}(t), x(t)) : \quad \xi(t, \dot{x}(t), x(t)) - \overline{\xi}(t, \dot{x}(t), x(t)) = 0. \tag{21}$$

Instead, if the variable of interest ξ is a *differential* variable, its evolution cannot be directly forced. Instead, its time derivative $\frac{d\xi}{dt}(t, \dot{x}(t), x(t))$ is specified by including the constraint

$$I(t, \dot{x}(t), x(t)) : \quad \frac{d\xi}{dt}(t, \dot{x}(t), x(t)) - \overline{\frac{d\xi}{dt}}(t, \dot{x}(t), x(t)) = 0 \tag{22}$$

in the set of DAEs.

2.4.2. Computation of worst-case battery operating modes

In this work, the definition of the battery operating mode needs to be further extended to account for uncertainty in the evolution of the state ξ, due to uncertainty affecting the parameters θ. Eqs. (21) and (22) can be rewritten for the probabilistic worst-case state evolution $\xi^{\text{w.c.}}(t)$, which in turn can be computed according to (18), leading to

$$I(t, \dot{x}(t), x(t)) : \quad \xi^{\text{w.c.}}(t, \dot{x}(t), x(t)) - \overline{\xi}(t, \dot{x}(t), x(t)) = 0; \tag{23}$$

$$I(t, \dot{x}(t), x(t)) : \quad \frac{d\xi^{\text{w.c.}}}{dt}(t, \dot{x}(t), x(t)) - \overline{\frac{d\xi}{dt}}(t, \dot{x}(t), x(t)) = 0. \tag{24}$$

The reminder of this section defines the worst-case battery operating modes analyzed in this work.

For the volume-specific constraints, let v be the index of the vth discrete volume along the principal dimension of the battery, with $v = 1$ being the volume at cathode/current collector interface, and $v = V_{tot}$ being the volume at the anode/current collector interface. For particle-specific constraints, let p be the index of the pth particle within a considered volume.

2.4.3. Nominal constant current (CC) mode

The current $I(t, \dot{x}(t), x(t))$ is an algebraic state of the DAEs and its time evolution is defined by

$$I(t, \dot{x}(t), x(t)) : \quad I(t, \dot{x}(t), x(t)) - \overline{I} = 0, \tag{25}$$

where $\overline{I}$ is the value of the constant current in CC mode.

Remark. It is not necessary to define a worst-case current operating mode. Although treated as a state for computational purposes, the current is an input to the battery easily specified by feedback control of the voltage, and is therefore not affected by model uncertainty.

2.4.4. Worst-case constant voltage (CV) mode

The cell voltage $V(t, \dot{x}(t), x(t))$ is an algebraic state, defined by

$$V(t, \dot{x}(t), x(t)) = \Phi_s(v, t, \dot{x}(t), x(t))|_{v=1} - \Phi_s(v, t, \dot{x}(t), x(t))|_{v=V_{tot}} \tag{26}$$

where Φ_s is the solid potential and $\overline{V}$ is the desired value of the constant voltage in CV mode. The current forcing the desired worst-case voltage evolution can be obtained with the constraint:

$$I(t, \dot{x}(t), x(t)) : \quad V^{\text{w.c.}}(t, \dot{x}(t), x(t)) - \overline{V} = 0 \tag{27}$$

where $V^{\text{w.c.}}$ is computed as discussed in Section 2.3.

2.4.5. Worst-case constant power (CP) mode

The cell power $P(t, \dot{x}(t), x(t))$ is an algebraic state, defined by

$$P(t, \dot{x}(t), x(t)) = V(t, \dot{x}(t), x(t)) \times I(t, \dot{x}(t), x(t)), \tag{28}$$

where $\overline{P}$ is the value of the desired constant power in CP mode. The current forcing the desired worst-case power evolution can be obtained with the constraint:

$$I(t, \dot{x}(t), x(t)) : \quad P^{\text{w.c.}}(t, \dot{x}(t), x(t)) - \overline{P} = 0 \tag{29}$$

where $P^{\text{w.c.}}$ is computed as discussed in Section 2.3.

2.4.6. Worst-case constant lithium-plating overpotential (CLO) mode

The lithium-plating overpotential $\eta_p(v, p, t, \dot{x}(t), x(t))$ is an algebraic state, defined by

$$\begin{aligned}\eta_p(v, p, t, \dot{x}(t), x(t)) =& \Phi_s(v, p, t, \dot{x}(t), x(t)) + \\ &- \Phi_e(v, t, \dot{x}(t), x(t)) + \Phi_n(\theta)\end{aligned} \tag{30}$$

where Φ_s is the particle solid potential, Φ_e is the electrolyte potential, Φ_n is the nucleation barrier. For the pth particle of the vth volume, the current forcing the desired worst-case lithium-plating overpotential evolution can be obtained with the constraint:

$$I(t, \dot{x}(t), x(t)) : \quad \eta_p^{\text{w.c.}}(v, p, t, \dot{x}(t), x(t)) - \overline{\eta}_p = 0 \tag{31}$$

where $\overline{\eta}_p$ is the desired constant value of the lithium-plating overpotential, and $\eta_p^{\text{w.c.}}$ is computed as discussed in Section 2.3.

2.4.7. Worst-case constant temperature (CT) mode

The averaged cell temperature $T_{avg}(t, \dot{x}(t), x(t))$ is a differential variable. The current resulting in a constant, worst-case cell temperature value can be obtained with the constraint:

$$I(t, \dot{x}(t), x(t)) : \quad \frac{dT_{avg}^{\text{w.c.}}(t, \dot{x}(t), x(t))}{dt} = 0 \tag{32}$$

where $T_{avg}^{\text{w.c.}}$ is computed as discussed in Section 2.3.

2.4.8. Worst-case constant electrolyte concentration (CCe) mode

The electrolyte lithium concentration $C_e(v, t, \dot{x}(t), x(t))$ is a differential variable. For the vth volume, the current resulting in a constant, worst-case electrolyte concentration value can be obtained with the constraint:

$$I(t, \dot{x}(t), x(t)) : \quad \frac{\partial C_e^{\text{w.c.}}(v, t, \dot{x}(t), x(t))}{\partial t} = 0 \tag{33}$$

where $C_e^{\text{w.c.}}$ is computed as discussed in Section 2.3.

2.4.9. Worst-case constant solid particle concentration (CCs) mode

The lithium concentration in the pth particle of the vth volume of the cell, $C_s(v, p, t, \dot{x}(t), x(t))$, is a differential variable. For the pth particle of the vth volume, the current resulting in a constant, worst-case lithium concentration value can be obtained with the constraint:

$$I(t, \dot{x}(t), x(t)) : \quad \frac{\partial C_s^{\text{w.c.}}(v, p, t, \dot{x}(t), x(t))}{\partial t} = 0 \tag{34}$$

where $C_s^{\text{w.c.}}$ is computed as discussed in Section 2.3.

2.5. Computation of safe fast charging protocols

This work focuses on the computation of safe, fast charging protocols for MPET models of lithium-ion batteries, able to guarantee probabilistically robust constraint satisfaction in presence of parametric model uncertainties. This task can be formulated as a *dynamic optimization* (Bryson & Ho, 2018; Srinivasan et al., 2003) of the form

$$\min_{t_f, u(t)} J(t_f, \dot{x}^*(t_f), x^*(t_f)) \tag{35}$$

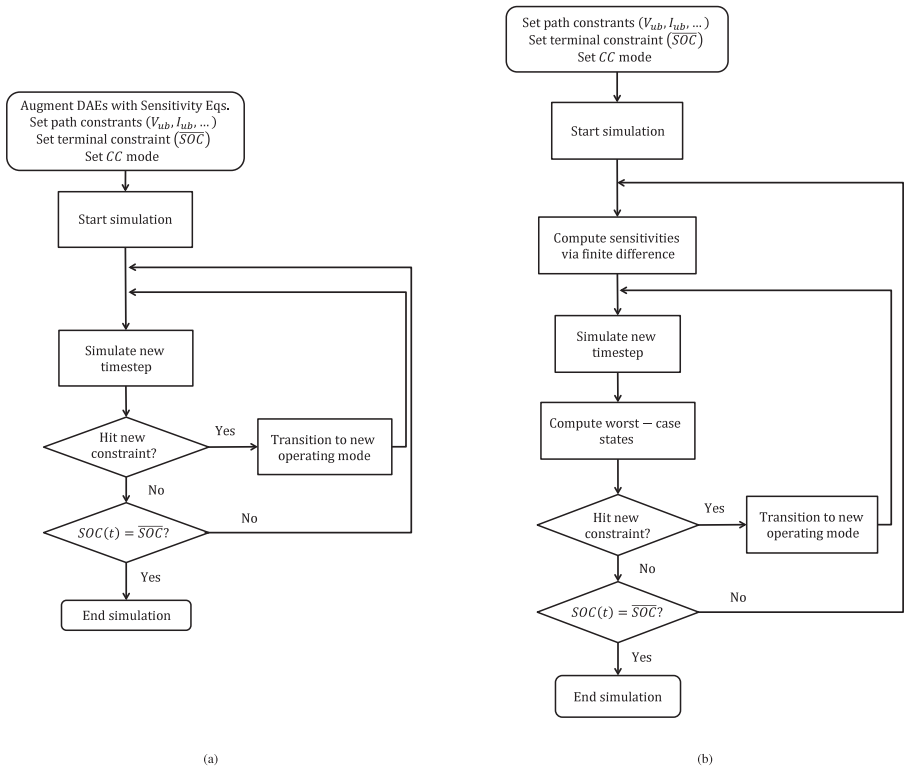

Fig. 1. Algorithm for the solution of the optimal charging problem, with worst-case states computed via (a) sensitivity equations or (b) finite differences.

subject to

$$F(t, \dot{x}^*(t), x^*(t), u(t)) = 0 \tag{36}$$

$$S(t, \dot{x}^{\text{w.c.}}(t), x^{\text{w.c.}}(t), u(t)) \leq 0 \tag{37}$$

$$T(t_f, \dot{x}^*(t_f), x^*(t_f), u(t_f)) \leq 0 \quad \forall\, 0 \leq t \leq t_f \tag{38}$$

where $J(t_f, \dot{x}^*(t_f), x^*(t_f))$ is the (nominal) objective function to be minimized, $u(t)$ is the control input (current), and t_f is the final time. Eq. (36) is a set of (consistently initialized) DAEs defining the nominal process model, (37) is a set of path constraints involving worst-case states, and (38) is a set of terminal constraints involving nominal states.

When dealing with the computation of fast charging protocols, terminal constraints and objective function encode the need to shorten the charging time as much as possible. A possible choice is $J = t_f$, with $t_f : \text{SOC}^*(t_f) = \overline{\text{SOC}}$ and $\overline{\text{SOC}}$ the desired state of charge to be reached. In this case, a *nominal* or *average* performance index is chosen. A probabilistic worst-case performance specification could be considered by, e.g., formulating the terminal constraint on the worst-case SOC. Safety constraints can be encoded in (37) by placing upper and/or lower bounds on current, worst-case voltage, worst-case power, etc. Worst-case state evolution can be obtained by propagating the uncertainty affecting model parameters by means of the procedure discussed in Section 2.3.[1]

The optimal charging problem could be numerically solved using nonlinear programming tools (Luenberger & Ye, 1984; Schlegel, Stockmann, Binder, & Marquardt, 2005). If a simplifying assumption is introduced, however, the optimization can be more efficiently solved by reformulating it as a *hybrid simulation* (Berliner et al., 2022a; Mosterman, 1999), where the model equations are changing as function of the states due to discrete events. Specifically, it is required that the optimal control input (i.e., the current I) is always forcing the states of the system along a path constraint, which are activated one at a time, until reaching the terminal constraint. This condition is stated formally as Assumption 1, which states that the optimal solution consists of a *sequence of battery operating modes*.

Assumption 1. Define switching times t_{sw} as the time instants in which the system transitions from one active constraint to the next:

$$\exists\, i_1, i_2 \text{ with } i_1 \neq i_2 \tag{39}$$

such that

$$S_{i_1}(t_{sw}^-, \dot{y}(t), y(t)) = 0 \text{ and } S_{i_2}(t_{sw}^-, \dot{y}(t), y(t)) \neq 0. \tag{40}$$

$$S_{i_1}(t_{sw}, \dot{y}(t), y(t)) = 0 \text{ and } S_{i_2}(t_{sw}, \dot{y}(t), y(t)) = 0. \tag{41}$$

$$S_{i_1}(t_{sw}^+, \dot{y}(t), y(t)) \neq 0 \text{ and } S_{i_2}(t_{sw}^+, \dot{y}(t), y(t)) = 0 \tag{42}$$

where S_i denotes the ith path constraint.

Assume that the optimal solution to the charging problem (35)–(38) satisfies the condition that, for each $t \in [0, t_f]$, $t \notin \mathcal{T}_{sw}$, there exists one and only one $i^*(t)$ such that $S_{i^*(t)}(t, \dot{y}(t), y(t)) = 0$, where $\mathcal{T}_{sw}$ is the set of switching times for the solution to the charging problem (35)–(38).

As analyzed in a general framework (Srinivasan et al., 2003), and specifically discussed for fast charging of lithium batteries (Berliner et al., 2022a), this assumption does not appear to be restrictive, and is well supported by many results available in the literature (see e.g., Kolluri et al., 2020; Mohtat et al., 2021; Perez et al., 2017; Pozzi et al., 2020; Zou et al., 2018). For Single Particle Models, it was proven in Berliner, Jiang, Cogswell, Bazant, and Braatz (2022b) that this assumption leads to almost optimal results.

The algorithm allowing the solution of an optimal charging problem via hybrid simulation is summarized with the flowcharts depicted in Figs. 1(a)b. When sensitivity equations are used to compute state sensitivities (Fig. 1(a)), the set of DAEs are first augmented with the corresponding sensitivity equations, and the safety and terminal constraints set as desired. The battery simulation starts in *CC* mode.

[1] The choice of the worst-case square root sign in (18) should be adapted to the case of upper or lower bound on each specific state.

The DAEs defining the nominal battery model in CC mode are solved forward in time along with the sensitivity equations. When a new constraint is hit by a worst-case state, the battery transitions to the operating mode associated with the new active constraint. Before resuming the simulation, the *CC* mode constraint is therefore replaced in the set of DAEs by a new constraint associated with the desired operating mode. This process is repeated every time a new constraint gets activated, until the terminal constraint is hit. On the other hand, in the case that the state sensitivities are computed by finite differences (Fig. 1(b)), the algorithm starts by setting the desired safety and terminal constraints, and starting a battery simulation in *CC* mode. At each iteration, state sensitivities are computed with the desired finite difference method (or set to a consistent initial value for the first iteration Galán et al., 1999). The set of DAEs is the solved forward in time for a time step, and worst-case states are computed by relying on sensitivities from the previous iteration. If a new constraint gets activated, before moving to the next time step, the set of DAEs is set up so that the battery transitions to the corresponding operating mode. The procedure is repeated until the terminal constraint is reached.

Remark. While in this work the methodology is presented and analyzed for MPET-based models, it can be straightforwardly applied to any battery model that can be cast as a set of DAEs.

3. Case study

This section applies the methodology for the computation of robust, safe fast charging protocols to a specific case study, which is described in the remainder of this section. Several charging protocols, involving different constraints, are computed and analyzed to demonstrate the effectiveness of the methodology, as well as the characteristics of each specific protocol.

3.1. Battery model

This work focuses on an MPET model of A123 System's (*A123 Systems official website*, 2023) *APR18650M1A* LFP batteries (nominal capacity of 1.1 Ah, charge cut-off voltage of 3.6 V, refer to Severson et al. (2019) for further details) as case study for the computation of robust, safe, fast charging protocols. The active materials used in the manufacturing of these cells exhibit a noticeable multiphase behavior. This motivates the choice of *APR18650M1A* LFP batteries as case study. As discussed in Section Section 2.1, MPET allows to accurately model charge and discharge of battery electrodes composed of phase separating materials with many particles. As observed in Fig. 4 of Smith and Bazant (2017), not only do microscopic variables such as particle concentration vary greatly between simple Newman (Newman & Tiedemann, 1975) models and multiphase models, but even macroscopic voltage measurements vary drastically when using simple Newman models compared to multiphase models for phase separating materials. In addition, phase separating materials often activate particle by particle (Dreyer, Guhlke, & Herrmann, 2011; Li et al., 2014) due to the many thermodynamic degrees of freedom in a phase separating population of particles, which solid solution models are incapable of capturing. These microscopic changes can greatly modify macroscopic voltage observations (Smith & Bazant, 2017). Thus, for phase separating materials, it becomes imperative to consider a multiphase many-particle model such as multiphase porous electrode theory.

Details regarding the MPET model (consisting of a system of 758 DAEs) are given in Table 1. The functional forms for the free energy and chemical potential of anode and cathode active materials (LiC_6 and $LiFePO_4$) are in the Appendix, while parameters of the Stefan–Maxwell electrolyte model can be found in Bernardi and Go (2011) and Valøen and Reimers (2005). A comparison of simulated and experimentally measured voltage profiles from (Severson et al., 2019) (Supplementary Fig. 27) is depicted in Fig. 2. Specifically, the proposed model well describes the experimental voltage trend for charging operations carried out at constant current, ranging from C/10 up to 8C. The agreement between experiment and simulations at high currents is acceptable although less accurate. Because of the unknown additives and coatings often used in commercial cells (Haregewoin, Wotango, & Hwang, 2016), perfect parameterization of the electrode kinetic and transport properties is extremely hard, especially at higher currents.

Table 1
Details of the MPET model used to simulate the behavior of A123 System's *APR18650M1A* LFP batteries.

Parameter name	Value
Nominal capacity	1.1 Ah
Charge cut-off voltage	3.6 V
Anode thickness	38 μm
Cathode thickness	79 μm
Separator thickness	25 μm
Anode loading fraction of active material	0.90
Cathode loading fraction of active material	0.84
Anode porosity	0.414
Cathode porosity	0.562
Separator porosity	0.4
Anode Bruggeman exponent	1.5
Cathode Bruggeman exponent	1.5
Separator Bruggeman exponent	1.5
Anode bulk conductivity	50 S/m
Cathode bulk conductivity	0.1 S/m
Anode # volumes	5
Cathode # volumes	50
Separator # volumes	5
Anode # particles per volume	4
Cathode # particles per volume	2
Anode particle shape	Spherical
Cathode particle shape	Rectangular
Anode particle size distribution	Weibull
Cathode particle size distribution	Lognormal
Anode particle size mean	6 μm
Cathode particle size mean	100 nm
Anode particle size standard deviation	2 μm
Cathode particle size standard deviation	20 nm
Anode particle reaction model	CHR
Cathode particle reaction model	ACR
Anode kinetics	Generalized BV
Cathode kinetics	Generalized BV
Anode reaction rate constant	30 A/m^2
Cathode reaction rate constant	0.16 A/m^2
Anode film resistance	5 $m\Omega/m^2$
Cathode film resistance	0 $m\Omega/m^2$
Nucleation barrier of Li plating	40 mV
Film resistance of Li plating	5 $m\Omega/m^2$
Anode active material	LiC_6
Cathode active material	$LiFePO_4$
Electrolyte model	Stefan–Maxwell
Electrolyte initial concentration	1.067 $kmol/m^3$
Anode heat capacity	700 J/(kg K)
Cathode heat capacity	700 J/(kg K)
Separator heat capacity	700 J/(kg K)
Separator heat transfer coefficient	1 $W/(m^2\ K)$

Remark. The multiphase modeling of the system includes the presence of a particle size distribution. Particles with different sizes become completely filled by lithium at different time instants (e.g., see Fig. 2), resulting in oscillations and small spikes in several battery states, which have been well established in the literature (Dreyer, Guhlke, & Herrmann, 2011; Dreyer, Guhlke, & Huth, 2011; Dreyer et al., 2010) and interpreted using MPET simulations (Ferguson & Bazant, 2014;

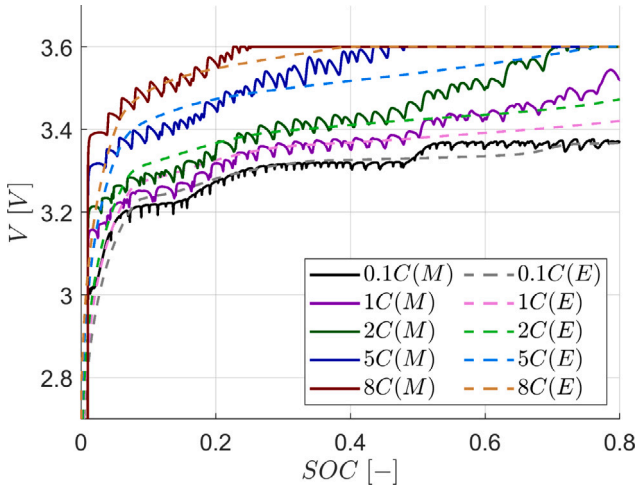

Fig. 2. Comparison of model and experimental voltage vs. SOC profiles under different constant current charging conditions (0.1C, 1C, 2C, 5C, 8C). The darker lines represent data from MPET simulations (M) and the lighter lines represent experimental data (E).

Li et al., 2014; Smith & Bazant, 2017). The finiteness of the number of particles in simulations causes the voltage spikes noted in these problems, as in the limit of infinite particles, the voltage spikes would tend to zero. Moreover, the size of particles also poses a lower limit to the spatial discretization of the electrodes (a finer discretization would further reduce spurious voltage oscillations and spikes). As such, it is not possible to completely remove the voltage spikes in MPET. In this case, the introduction of a small tolerance on constraint activation may be useful to reduce repeated switches between different operating modes, and favors the design of a smoother current profile for the charging protocol (Galuppini, Berliner, Lian, et al., 2023). Moreover, the evolution of state uncertainty may also be characterized by oscillations and spikes (e.g., see Fig. 3). In case of uncertainty propagation based on a finite difference sensitivity approach, it is important to define a sufficiently small time step for the update of uncertainties. This is fundamental to provide an accurate description of state uncertainty evolution and, at the same time, improve the ability of the control system to properly compensate for the effect of uncertainty. In this work, an update time step of 0.5 s was chosen, so that worst-case states do not exceed the tolerance already introduced on constraint activation.

Remark. The actual output of the methodology is not a sequence of operating modes, since some of them may not be enforced on the real system (e.g., CLO or CCe), but rather the current profile, which can instead be applied to the cell by means of a simple current control loop. Therefore, sudden switching in the active operating modes do not represent a real issue if they not generate wide current oscillation. The charging protocol can be *interpreted* as a sequence of operating modes, to provide further insight in the evolution of battery states resulting from the current profile.

3.2. Parametric model uncertainty

In this work, uncertainty is assumed to affect four model parameters. As more than 90% of the available algorithms to estimate parameters from experimental data produce normal distributions (Nagy & Braatz, 2007), uncertain parameters are assumed to be normally distributed. Specifically, the separator heat transfer coefficient h_h, anode reaction rate constant k_0^a, initial electrolyte concentration c_0^e, and lithium-plating nucleation barrier V_{nuc} are distributed as

$$h_h \sim \mathcal{N}(1, 0.025) \tag{43}$$

$$k_0^a \sim \mathcal{N}(40, 5) \tag{44}$$

$$c_0^e \sim \mathcal{N}(1100, 50) \tag{45}$$

$$V_{nuc} \sim \mathcal{N}(0.06, 0.0005) \tag{46}$$

For all protocols, a significance level $\alpha = 0.05$ is considered to ensure 95% probability of constraint satisfaction at each time instant.

Remark. In this work, the choice of the uncertain parameters is carried out so that uncertainty propagates to all the battery state subject to safety or operational constraints. Broadly speaking, the characterization of parameter uncertainties for (M)PET-like models must be carefully carried out at the parameter identification phase. As a matter of fact, (M)PET models may suffer from identifiability issues (Berliner, Zhao, et al., 2021; Galuppini, Berliner, Cogswell, et al., 2023). If not properly handled (e.g., by using informative prior distributions, or by fixing parameter values), unidentifiable parameters may be associated with uniform distributions and large variance values. Once such uncertainty propagates to the battery states, it may be very difficult to satisfy constraints with a small significance level.

4. Results

This section discusses the computation of five different protocols, by relying on the battery operating modes defined in Section 2.4. Table 2 summarizes the main features of each protocol. Figs. 3–7 depict the behavior of the main states of interest (voltage, current, state of charge, power, average cell temperature, lithium-plating overpotential, solid particle concentration and electrolyte concentration) for each protocol. As lithium-plating overpotential and average cell temperature are responsible for battery performance degradation (Berliner et al., 2022a), these quantities are given a specific attention in the analysis of results. Specifically, to preserve battery lifetime, lithium-plating overpotential should not reach negative values, while the cell temperature should not increase too much during charge operations.

4.1. Current and voltage constraints

This section discusses the design of a robust, safe, fast charging protocol considering standard current and voltage upper bounds. To obtain the protocol, the algorithm in Section 2.5 is used to compute the solution of the dynamic optimization:

$$t_f^O = \min_{t_f} \; t_f \tag{47}$$

subject to

$$F(t, \dot{x}(t), x(t)) = 0 \tag{48}$$

$$I^{\text{w.c.}}(t) \leq 8 \text{ C} \tag{49}$$

$$V^{\text{w.c.}}(t) \leq 3.6 \text{ V} \tag{50}$$

$$\text{SOC}^*(t_f) = 0.7 \tag{51}$$

$$\forall\, 0 \leq t \leq t_f$$

where 1% tolerance is allowed for constraint activation. In the reminder of this paper, denote this protocol as CC-CV. The time evolution of the states of is depicted in Fig. 3. Current is quickly ramped from 0 to its maximum value of 8C, and a CC charging phase begins. After about 103 s, the worst-case voltage hits its upper bound (at this point of the simulation, uncertainty in the voltage is still negligible) and a CV phase begins, and lasts until the terminal constraint on the SOC is met. The ability of the proposed stochastic optimal control approach to provide probabilistically robust constraint satisfaction is clearly shown in the time interval between 350 and 450 s. As uncertainty affecting the voltage grows or diminishes, the input current forces the nominal voltage to back off or become closer to the corresponding constraint, so that worst-case voltage evolution is kept constant, and the constraint active.

Table 2
Charging protocols and associated charging times.

Protocol	Mode 1 duration [s]	Mode 2 duration [s]	Mode 3 duration [s]	Mode 4 duration [s]	Mode 5 duration [s]	Mode 6 duration [s]	Mode 7 duration [s]	Charging time [s]
CC-CV	CC(103.14)	CV(4.24)	CC(2.77)	CV(426.89)	NA	NA	NA	537.0355
CC-CP-CV	CC(1.10)	CP(297.08)	CV(10.19)	CP(7.14)	CV(17.36)	CP(1.40)	CV(266.35)	600.6273
CC-CT-CV	CC(86.35)	CT(263.49)	CV(1.00)	CT(22.00)	CV(5.33)	CT(11.00)	CV(232.28)	621.4406
CC-CLO-CV	CC(103.14)	CV(4.24)	CC(2.77)	CV(320.00)	CLO(1.50)	CV(10.48)	CLO(537.91)	980.0339
CC-CCe	CC(4.22)	CCe(1861.29)	NA	NA	NA	NA	NA	1865.511

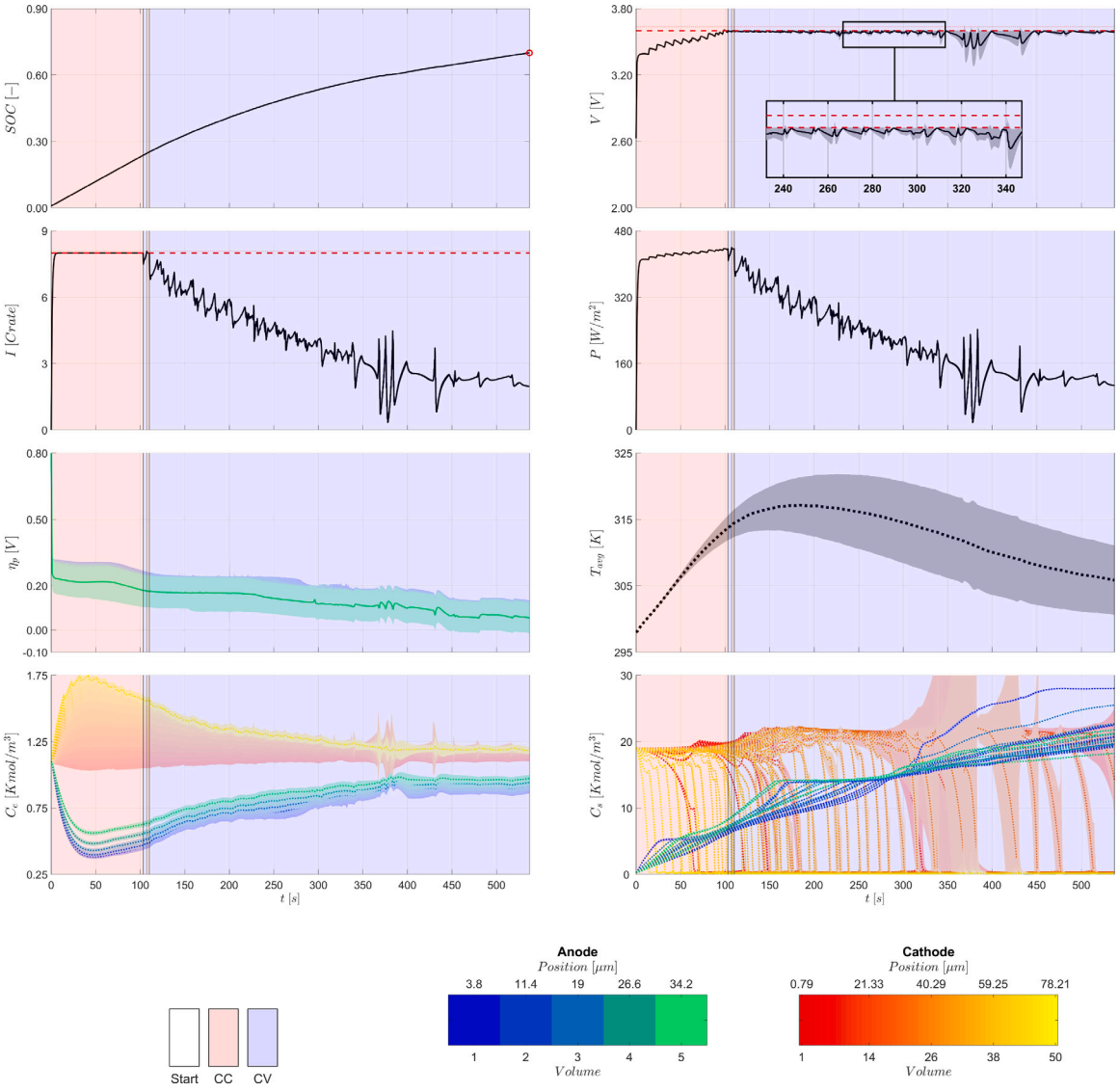

Fig. 3. CC-CV Protocol. Time evolution of SOC, voltage V, current I, power P, lithium-plating overpotential η_p, spatially averaged cell temperature T_{avg}, electrolyte concentration C_e, and solid particle concentration C_s. Nominal/average values are depicted as thick lines, and the corresponding uncertainties as shaded areas. Thick red, dashed lines represent nominal constraints, while thin, red dotted lines represent constraints relaxed including a 1% tolerance.

4.2. Current, voltage and power constraints

This section discusses the design of a robust, safe, fast charging protocol considering current, voltage, and power upper bounds. To obtain the protocol, the algorithm in Section 2.5 is used to compute the solution of the dynamic optimization:

$$t_f^O = \min_{t_f} \; t_f \tag{52}$$

subject to

$$F(t, \dot{x}(t), x(t)) = 0 \tag{53}$$

$$I^{\text{w.c.}}(t) \leq 8 \text{ C} \tag{54}$$

$$V^{\text{w.c.}}(t) \leq 3.6 \text{ V} \tag{55}$$

$$P^{\text{w.c.}}(t) \leq 270 \text{ W/m}^2 \tag{56}$$

$$\text{SOC}^*(t_f) = 0.7 \tag{57}$$

$$\forall\, 0 \leq t \leq t_f$$

where 1% tolerance is allowed for constraint activation. In the reminder of this paper, denote this protocol as CC-CP-CV. The time evolution of the states of interest is depicted in Fig. 4. The simulation starts by ramping the current from 0 to its maximum value. During the ramp,

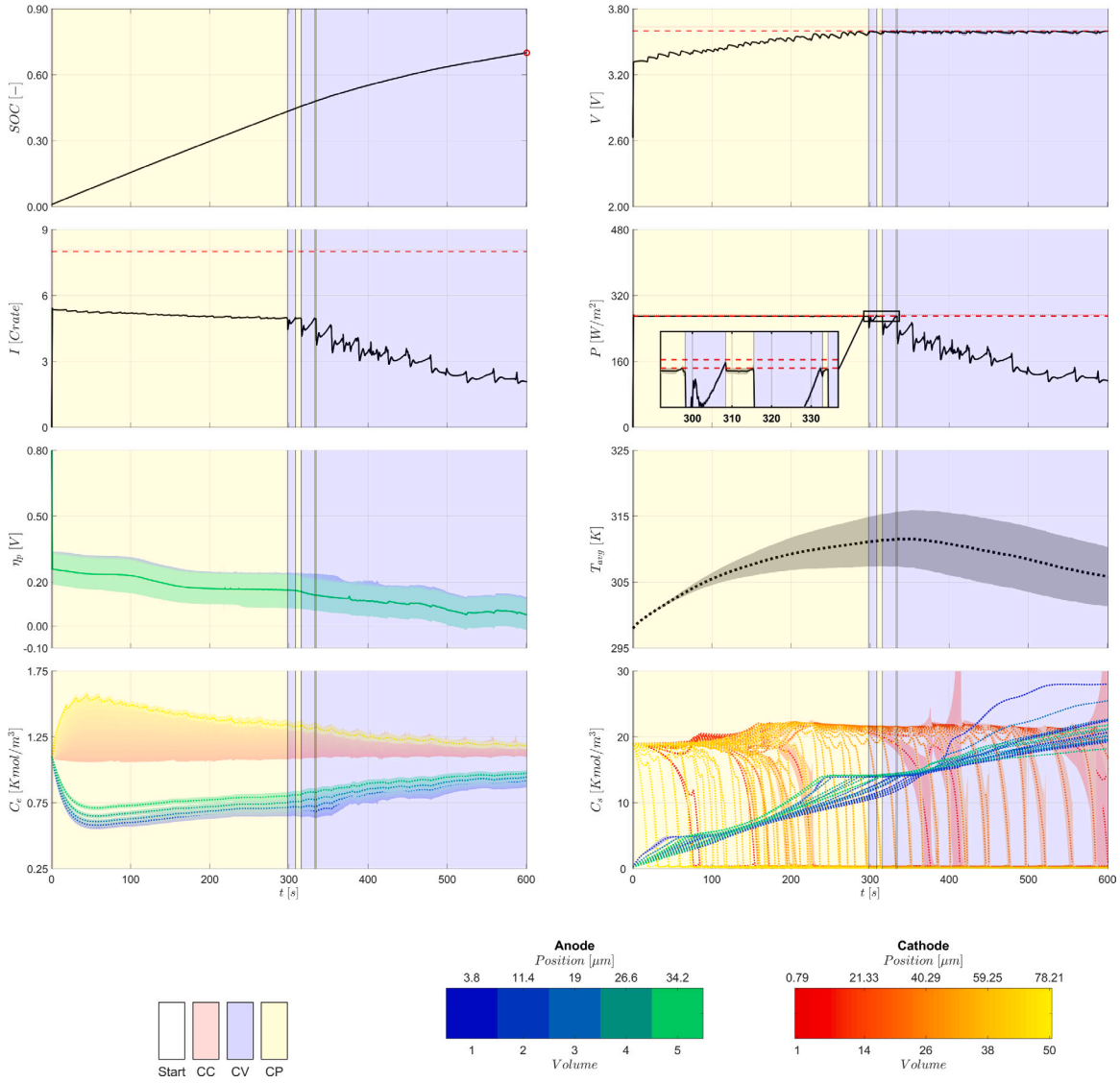

Fig. 4. CC-CP-CV Protocol. Time evolution of SOC, voltage V, current I, power P, lithium-plating overpotential η_p, spatially averaged cell temperature T_{avg}, electrolyte concentration C_e, and solid particle concentration C_s. Nominal/average values are depicted as thick lines, and the corresponding uncertainties as shaded areas. Thick red, dashed lines represent nominal constraints, while thin, red dotted lines represent constraints relaxed including a 1% tolerance.

the worst-case power constraint is activated, and the simulation almost immediately transitions to the CP state, which remains steadily active for about half of the charging operations (about 297 s). A this point, worst-case voltage hits its upper bound and triggers a switch to the CV phase. Due to oscillations in both voltage and power, CP and CV operating modes alternate in the following 30 s, until a steady CV phase is reached to conclude the charging operations. Interestingly, when comparing the results to the CC-CV case previously analyzed, the uncertainty affecting voltage is reduced, due to the different input current evolution. This further stresses the advantage of the proposed methodology over the use of constant backoff values for constraints, which would likely result in over conservative constraint tightening and, in turn, in poorer performance of the corresponding charging protocol.

4.3. Current, voltage and temperature constraints

This section discusses the design of a charging protocol considering upper bounds on the current, voltage, and average cell temperature. This can be useful to prevent excessive cell heating, which is known to reduce battery lifetime. The charging protocol is obtained as the solution of the dynamic optimization:

$$t_f^O = \min_{t_f} \; t_f \tag{58}$$

subject to

$$F(t, \dot{x}(t), x(t)) = 0 \tag{59}$$

$$I^{\text{w.c.}}(t) \leq 8 \text{ C} \tag{60}$$

$$V^{\text{w.c.}}(t) \leq 3.6 \text{ V} \tag{61}$$

$$T_{avg}^{\text{w.c.}}(t) \leq 310 \text{ K} \tag{62}$$

$$\text{SOC}^*(t_f) = 0.7 \tag{63}$$

$$\forall\, 0 \leq t \leq t_f$$

where 1% tolerance is allowed for constraint activation. In the reminder of this paper, denote this protocol as CC-CT-CV. The time evolution of the states of interest is depicted in Fig. 5. As for the CC-CV protocol, charging operations begin with a steady CC phase, lasting about

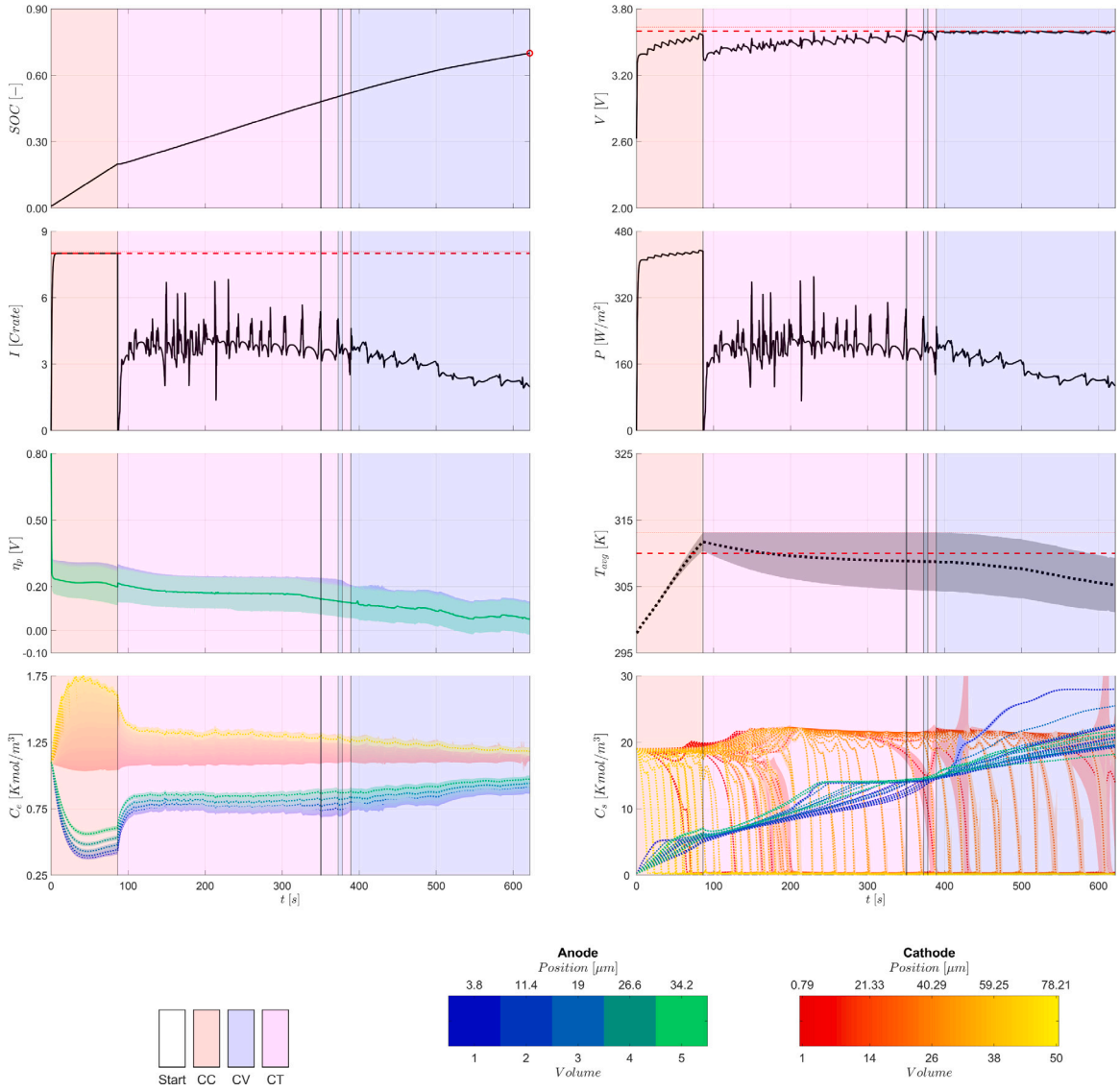

Fig. 5. CC-CT-CV Protocol. Time evolution of SOC, voltage V, current I, power P, lithium-plating overpotential η_p, spatially averaged cell temperature T_{avg}, electrolyte concentration C_e, and solid particle concentration C_s. Nominal/average values are depicted as thick lines, and the corresponding uncertainties as shaded areas. Thick red, dashed lines represent nominal constraints, while thin, red dotted lines represent constraints relaxed including a 1% tolerance.

86 s. As worst-case average temperature activates the corresponding constraint, the system switches to CT operating mode, which forces constant evolution of worst-case average temperature. To achieve this, as uncertainty affecting the temperature is constantly increasing, the temperature is progressively lowered. Charging operations are nearly stopped (current goes to 0) during the CC to CT switching instant, to prevent the temperature from increasing further and violating the constraint. Charging operations are then resumed at a mild current value, progressively decreasing. Finally, charging operations switch to CV and, after briefly alternating between CV and CT, reach a steady CV operating mode, which concludes the simulation.

Remark. Recall that, as temperature is a differential state of the battery, it is not possible to control its instantaneous value, but only its time derivative. The CT operating mode therefore freezes temperature at the value at the time the CT operating mode is activated. Due to the presence of a deadband on constraint activation, the CT operating mode keeps the worst-case temperature constantly equal to the *relaxed* constraint value, as depicted in Fig. 5.

4.4. Current, voltage and lithium-plating overpotential constraints

This section discusses the design of a charging protocol considering upper bounds on current and voltage and a lower bound on lithium-plating overpotential. Side reactions triggered by negative values of the lithium-plating overpotential contribute to degradation of the battery. Constraining the lithium-plating overpotential to a lower bound can prevent this degradation mechanism from occurring. To obtain the protocol, the algorithm in Section 2.5 is used to compute the solution of the dynamic optimization:

$$t_f^O = \min_{t_f} \; t_f \tag{64}$$

subject to

$$F(t, \dot{x}(t), x(t)) = 0 \tag{65}$$

$$I^{\text{w.c.}}(t) \leq 8 \text{ C} \tag{66}$$

$$V^{\text{w.c.}}(t) \leq 3.6 \text{ V} \tag{67}$$

$$\eta_p^{\text{w.c.}}(t, v_a, p_a) \geq 0.01 \text{ V} \tag{68}$$

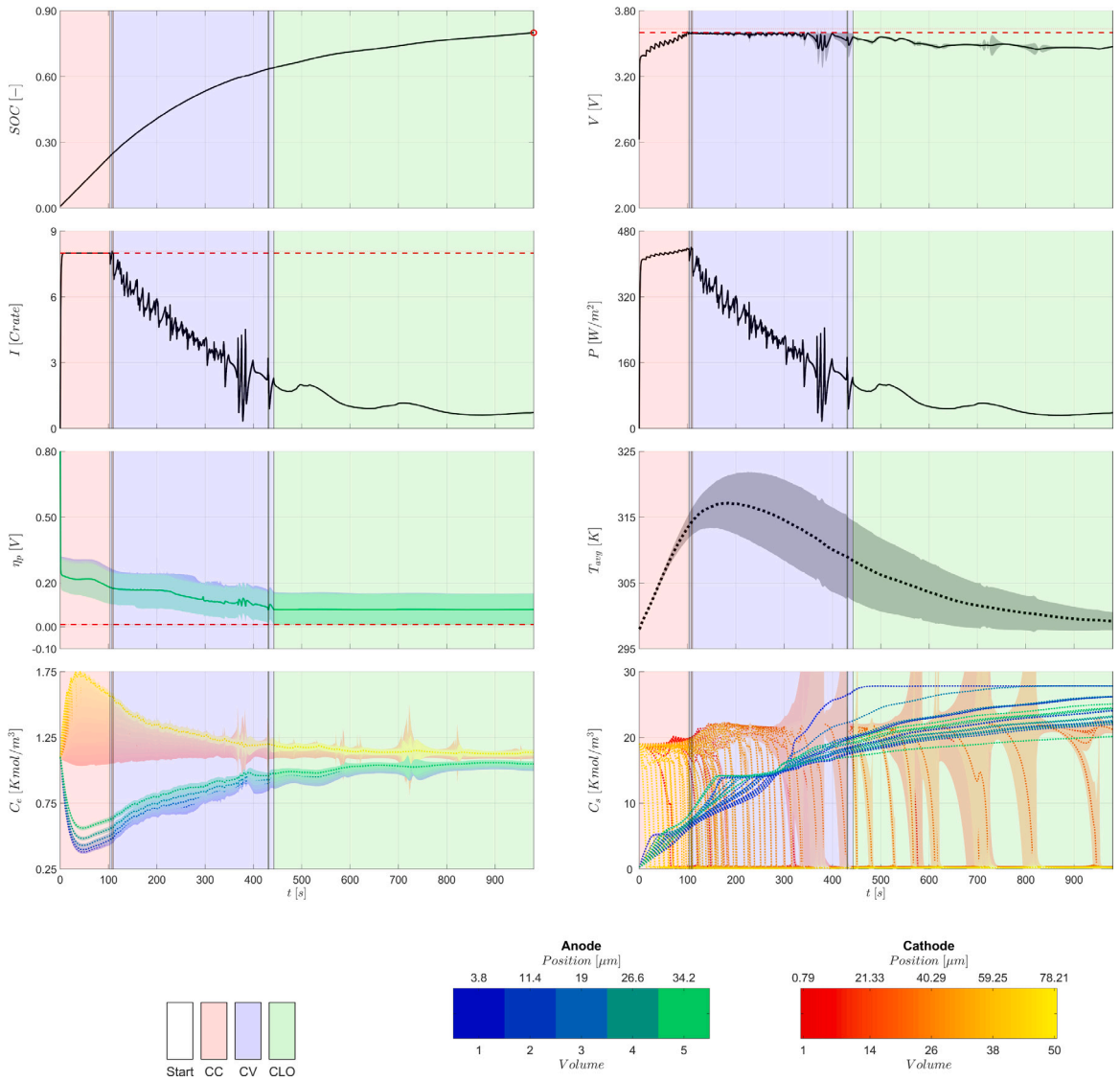

Fig. 6. CC-CLO-CV Protocol. Time evolution of SOC, voltage V, current I, power P, lithium-plating overpotential η_p, spatially averaged cell temperature T_{avg}, electrolyte concentration C_e, and solid particle concentration C_s. Nominal/average values are depicted as thick lines, and the corresponding uncertainties as shaded areas. Thick red, dashed lines represent nominal constraints, while thin, red dotted lines represent constraints relaxed including a 1% tolerance.

$$\begin{aligned} \mathrm{SOC}^*(t_f) &= 0.8 \\ \forall\, 0 \le t \le t_f & \\ v_a &= 5 \\ p_a &= 1,2,3,4 \end{aligned} \tag{69}$$

where 1% tolerance is allowed for constraint activation. In the reminder of this paper, denote this protocol as CC-CLO-CV. All of the particles in the last volume of the anode (that is, at the anode/separator interface) are required to fulfill the lower bound on lithium-plating overpotential. The time evolution of the states of interest in the solution is depicted Fig. 6. Up to about 450 s, the battery evolution coincides with that of the CC-CV protocol analyzed earlier in this section. In contrast, as worst-case lithium-plating overpotential hits its lower bound, the system transitions to CLO mode, which lasts for about 500 s and concludes charging operations. Interestingly, current shows a much smoother profile during the CLO phase.

4.5. Current, voltage and electrolyte concentration constraints

This section discusses the design of a charging protocol considering upper bounds on the current and voltage, a lower bound on the electrolyte concentration $C_e(t, v_a, v_c)$ in each volume of the anode, and an upper bound on the solid concentration of anode particles. To obtain the protocol, the algorithm in Section 2.5 is used to compute the solution of the dynamic optimization:

$$t_f^O = \min_{t_f}\ t_f \tag{70}$$

subject to

$$F(t, \dot{x}(t), x(t)) = 0 \tag{71}$$

$$I^{\mathrm{w.c.}}(t) \le 8\ \mathrm{C} \tag{72}$$

$$V^{\mathrm{w.c.}}(t) \le 3.6\ \mathrm{V} \tag{73}$$

$$C_e^{\mathrm{w.c.}}(t, v_a, v_c) \ge 930\ \mathrm{mol/m^3} \tag{74}$$

$$C_s^{\mathrm{w.c.}}(t, v_a, p_a) \le 27940\ \mathrm{mol/m^3} \tag{75}$$

$$\begin{aligned} \mathrm{SOC}^*(t_f) &= 0.7 \\ \forall\, 0 \le t \le t_f & \\ v_a &= 1,2,\dots,5 \\ v_c &= 1,2,\dots,50 \\ p_a &= 1,2,3,4 \end{aligned} \tag{76}$$

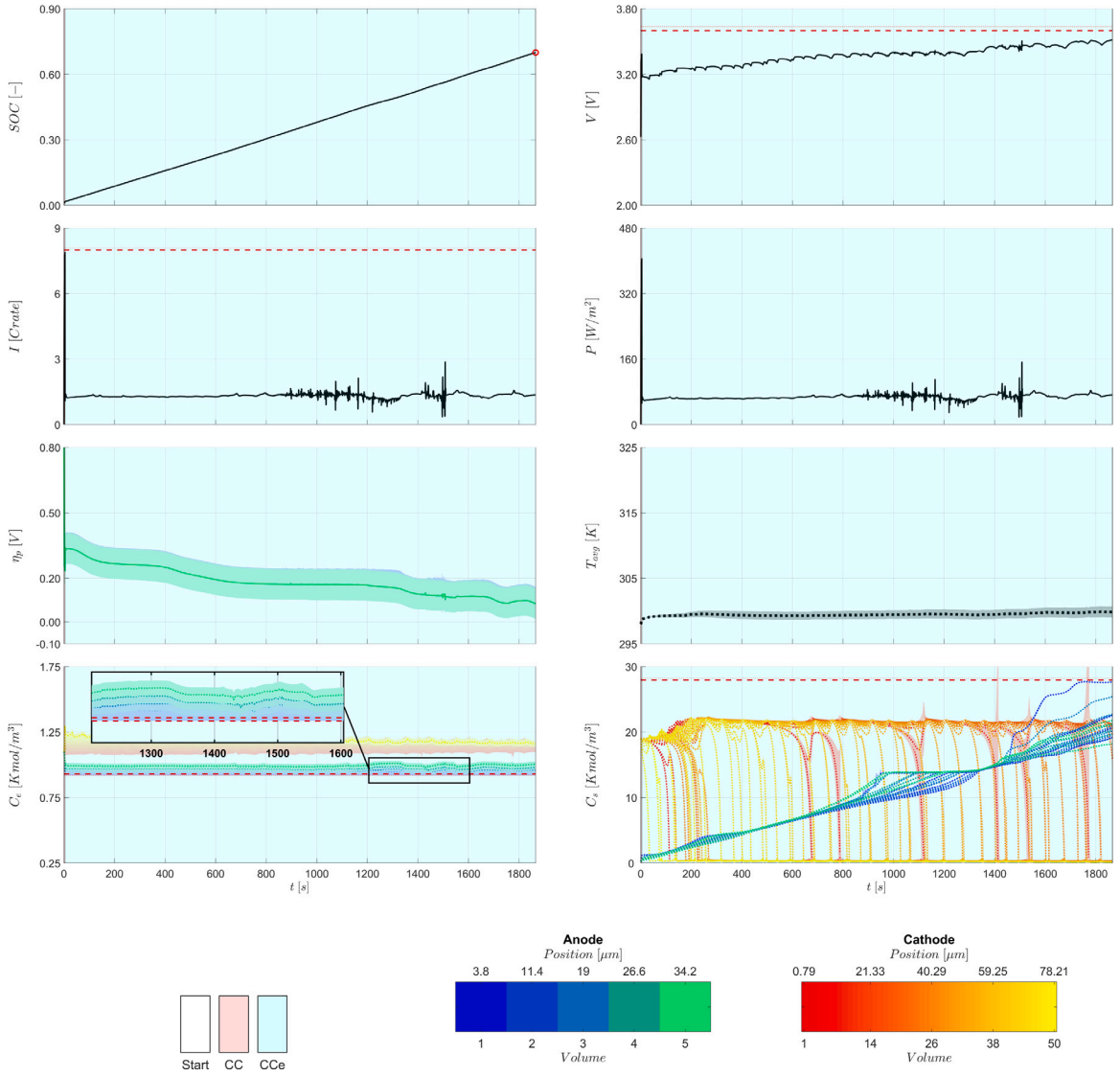

Fig. 7. CC-CCe Protocol. Time evolution of SOC, voltage V, current I, power P, lithium-plating overpotential η_p, spatially averaged cell temperature T_{avg}, electrolyte concentration C_e, and solid particle concentration C_s. Nominal/average values are depicted as thick lines, and the corresponding uncertainties as shaded areas. Thick red, dashed lines represent nominal constraints, while thin, red dotted lines represent constraints relaxed including a 1% tolerance.

where 1% tolerance is allowed for constraint activation. In the reminder of this paper, denote this protocol as CC-CCe. The time evolution of the states of interest is depicted in Fig. 7. In this case, the initial CC phase only lasts for few seconds, as the lower bound on worst-case electrolyte concentration is soon activated. From 8C, current quickly ramps down to about 1C, and the system moves to the CCe operating mode, which forces a constant evolution of the worst-case electrolyte concentration. To achieve this, current reacts to oscillations in both electrolyte concentration and in its uncertainty. The CCe phase lasts until the end of charging operations. Again, as already underlined for the CC-CP-CV protocol, charging operations performed at lower C-rate values seem to reduce the rate at which uncertainty propagates from parameters to states (in this case, uncertainty affecting voltage and power remains negligible during the whole simulation). The worst-case electrolyte concentration is forced to assume the relaxed constraint value (see Fig. 7), as electrolyte concentration is a differential state of the battery. The upper bound on the worst-case solid particle concentration was never activated during the simulation.

5. Discussion

As demonstrated in the previous section, the proposed stochastic optimal control approach can effectively be used to compute safe, fast charging protocols for (possibly multiphase) lithium-ion batteries, based on dynamic models affected by parametric uncertainties. The protocols obtained in this way guarantee a user-defined probability of constraint satisfaction at each time instant.

While this work focuses on *probabilistically robust* constraint satisfaction, the proposed methodology can be straightforwardly adapted to guarantee *robust* constraint satisfaction. In the latter case, parametric uncertainty should be described by a generalized ball, defined by means of an appropriate p-norm (e.g., 1-norm or ∞-norm). This representation includes the case of an uncertainty hyper-box, with known hard lower and upper bounds on model parameters (Nagy & Braatz, 2004, 2007). The same power series expansion techniques can then be applied to propagate uncertainty to model states and, in the case of first-order expansion, analytically compute worst-case state deviations which can be used as backoff terms in the dynamic optimization (Nagy & Braatz, 2004, 2007).

Table 3
Computation times of charging protocols using the proposed hybrid simulation approach (T_{HS}) and an Intel® Core™ 2.60 GHz i7-6700HQ CPU, and estimate of computation times using a gradient descent algorithm ($\hat{T}_{HS}$).

Protocol	T_{HS} [s]	$\hat{T}_{HS}$ [s]
CC-CV	28,286	230,695,200
CC-CP-CV	29,809	288,000,000
CC-CT-CV	32,264	308,512,800
CC-CLO-CV	49,374	768,320,000
CC-CCe	107,792	2,782,580,000

An alternative to the power series technique adopted in this work is polynomial chaos expansions (Nagy & Braatz, 2004, 2007). Polynomial chaos expansions are well suited to designing systems to be robust to uncertainties when the objectives are strongly dependent on the shape or tails of probability distributions of the uncertainties. In contrast, sampling-based uncertainty propagation techniques such as Monte Carlo methods can produce extremely accurate results, at the price of a much higher computational cost, which may not be affordable for this specific application (Nagy & Braatz, 2004, 2007). Monte Carlo methods can be used offline to confirm the accuracy of power series or polynomial chaos expansions techniques (Nagy & Braatz, 2007).

The methodology could be straightforwardly extended to consider robust or probabilistic worst-case performance. While a *nominal* or *average* performance specification is chosen for this work, a robust specification could be considered by formulating the terminal constraint on the worst-case SOC instead of the nominal SOC.

Regardless of the robust or stochastic formulation of the optimal control problem, the main advantage of the approach proposed in this work lies in the dynamic, model-based computation of backoff values for constraint tightening. As the simulations clearly show, the dynamics of uncertainty propagation from parameters to states can be strongly dependent on the input current. The proposed methodology reduces conservatism with respect to standard, constant backoff approaches by computing, at each time instant, minimum backoff values guaranteeing constraint satisfaction.

Table 3 reports the time required to compute each protocol with the hybrid simulation approach, T_{HS}, using an Intel® Core™ 2.60 GHz i7-6700HQ CPU. While the computing times are not suitable for an *online* protocol computation, the proposed approach makes the optimal control problem computationally tractable for offline computations. Table 3 also reports the estimated cost for computing a charging protocol via the widely used approach of *control vector parameterization* (Luenberger & Ye, 1984). In this approach, a parameterization is chosen for the control signal (current) with the typical choice being piecewise constant with time intervals of predefined length. The restriction of the search space results in suboptimality which can be reduced by increasing the number of time intervals.[2] The proposed hybrid simulation approach also reduces the search space, as specified in Assumption 1, to reduce the computational cost by replacing the optimization by hybrid simulation. In contrast to control vector parameterization, our proposed approach allows the control action (current) to evolve very rapidly, and with arbitrary shapes. Furthermore, the computation times for our proposed approach are more than a 1000-fold shorter.

The estimated computational cost for control vector parameterization in Table 3, $\hat{T}_{GD}$, assumes the use of a sequential, Newton-type gradient descent optimization algorithm. The number of optimization variables involved in the computation of each protocol, n_O, is $n_O \approx t_f^O/T_s$, where T_s is the sampling time of the control action and t_f^O is the charging time. In our comparison, we set $T_s = 0.5$ s equal to the update time for backoff values used with the hybrid simulation approach, and t_f^O as the charging time obtained with the hybrid simulation approach (see Table 2). Assuming

- a first-order optimization algorithm is used (Nesterov & Nemirovskii, 1994),
- the gradient is computed via first-order finite differences (Luenberger & Ye, 1984),
- the linearized sensitivity is computed via central finite difference (Luenberger & Ye, 1984),

and making the optimistic estimate that only 100 gradient calculations are needed for convergence, the estimated overall computational time is $\hat{T}_{GD} \approx 100 n_O (2 T_e n_u)$, where the execution time T_e of an MPET simulation is about 1/2 of the simulation horizon, which is equal to the charging time t_f^O, and n_u is the number of uncertain parameters in the MPET model.

The proposed methodology for the solution of the stochastic optimal control problem could also be used in combination with a state observer and the receding/shrinking horizon principle, in an (output feedback) MPC strategy. The online computational cost could be reduced by replacing MPET with a reduced-order model.

If all system states subject to constraints can be measured or estimated (e.g., current and voltage), and the corresponding operating modes enforced in practice by means of lower level control loops, the proposed procedure to solve the dynamic optimization can be used to compute the charging protocol on the flight, directly acting on the real system.[3] Uncertainty affecting output measurements and state estimates can be accommodated using suitable backoff values. In this case, the robust/stochastic dynamic optimization formulation does not explicitly require a model of the entire system, as online measurements or estimates the system states would be used instead.

6. Conclusions

This work proposes an efficient optimal control approach for computing safe, fast charging protocols for lithium-ion batteries, in the presence of parametric model uncertainties. Based on a stochastic description of uncertainty affecting the model parameters, the methodology ensures probabilistically robust satisfaction of safety constraints by first propagating uncertainty to the system states, and then computing, at each time instant, suitable backoff values for constraint tightening in the optimal control problem formulation.

Uncertainty propagation is carried out by means of sensitivity analysis and power series expansion. The resulting optimal control problem can be reformulated as a hybrid simulation and efficiently solved. The proposed solution always consists of a sequence of battery operating modes. In this work, the methodology is tested by computing several fast charging protocols for a commercially available LFP battery (A123 System's *APR18650M1A*), which is characterized by multiphase behavior. A detailed MPET model is used for the computation of charging protocols. The simulation results demonstrate the effectiveness of the approach and it ability to explicitly incorporate complex battery models.

Funding

This work was supported by the Toyota Research Institute, USA through the D3BATT Center on Data-Driven-Design of Rechargeable Batteries.

[2] An alternative approach to computing a charging protocol explicitly considers the *optimality conditions* of the optimal control problem (Bryson & Ho, 2018; Srinivasan et al., 2003). This methodology does not introduce any suboptimality, but is computationally very expensive.

[3] That is, replacing the computer simulation by the operation of the real physical system.

Code Availability

All the software code related to this work is available online at https://github.com/GiacomoGaluppini?tab=repositories.

Declaration of competing interest

The authors declare that they have no known competing financial interests or personal relationships that could have appeared to influence the work reported in this paper.

Appendix. Parameters for the phase-field model

The parameters for the phase-field model including the chemical potential and diffusion coefficient are presented in this section. The phase-field model for lithium intercalation compounds are adapted from (Bai, Cogswell, & Bazant, 2011; Smith & Bazant, 2017) with modifications to comply with experiments.

In the phase-field model for lithium intercalation of the graphite, the chemical potential is the function of the local filling fraction or dimensionless concentration $\tilde{c} = c/c_{\max}^{(\text{graphite})}$, given by

$$\mu(\tilde{c}) = \mu_{\text{h}}(\tilde{c}) - \kappa\nabla^2\tilde{c} \tag{A.1}$$

where μ_{h} is the part of chemical potential fitted to reproduce the open-circuit voltage of the graphite while capturing the phase separation behavior of graphite, and κ is the gradient energy penalty. The functional form of μ_{h} is adapted from previous work (Smith & Bazant, 2017) and given by

$$\begin{aligned}\mu_{\text{h}}(\tilde{c})/(k_{\text{B}}T) =& 0.18 + S_{\text{D}}(\tilde{c}, 0.35, 0.05)[-40e^{-\tilde{c}/0.015} \\ &- 1.5S_{\text{D}}(\tilde{c}, 0.17, 0.02) - 2S_{\text{D}}(\tilde{c}, 0.22, 0.04)] \\ &- \frac{0.05}{\tilde{c}^{0.85}} + 10S_{\text{U}}(\tilde{c}, 1, 0.045) \\ &+ 6.12(0.4 - \tilde{c})S_{\text{D}}(\tilde{c}, 0.49, 0.045)S_{\text{U}}(\tilde{c}, 0.35, 0.05) \\ &+ [3.4(0.74 - \tilde{c}) + 1.26]S_{\text{U}}(\tilde{c}, 0.5, 0.02)\end{aligned} \tag{A.2}$$

where the step-up function S_{U} and step-down function S_{D} are given by

$$\begin{aligned}S_{\text{U}}(\tilde{c}, x_c, \delta) &= 0.5\left(\tanh\left(\frac{\tilde{c} - x_c}{\delta}\right) + 1\right), \\ S_{\text{D}}(\tilde{c}, x_c, \delta) &= 0.5\left(-\tanh\left(\frac{\tilde{c} - x_c}{\delta}\right) + 1\right).\end{aligned} \tag{A.3}$$

The last line of (A.2) is slightly different from our previous work (Smith & Bazant, 2017) by further penalizing the homogeneous phase during the Stage II-I phase separation so that the phase separation is not suppressed during high charging rate, in accordance to the experiments.

The functional form of tracer diffusion coefficient in the graphite is taken from the DFT calculation that characterizes its concentration dependence (Persson, Hinuma, Meng, Van der Ven, & Ceder, 2010). Its magnitude was treated as a fitting parameter to account for the effective diffusion path inside a secondary graphite particle so that

$$D(\tilde{c}) = \tilde{D}D_0(\tilde{c}) \tag{A.4}$$

where $\tilde{D}$ is a scalar fitting parameter and $D_0(\tilde{c})$ is given by

$$D_0(\tilde{c})\ (\text{cm}^2/\text{s}) = \begin{cases} 10^{-8.0\tilde{c}-5.6}, & 0 < \tilde{c} < 1/2, \\ 10^{-2.8\tilde{c}-6.5}, & 1/2 < \tilde{c} < 1. \end{cases} \tag{A.5}$$

In the phase-field model for lithium intercalation of the $LiFePO_4$, the depth-averaged model is used and resulting in an ACR-type phase-field model (Bai et al., 2011). The chemical potential is adapted from a regular solution type model and then adjusted to fit the open-circuit voltage at the low filling fractions, which is given by

$$\begin{aligned}\mu_{\text{h}}(\tilde{c})/(k_{\text{B}}T) =& -15e^{-\tilde{c}/0.005} \\ &+ (1.9 - 2.0\tilde{c} - 2.0\tilde{c}^2)S_{\text{U}}(\tilde{c}, 0.03, 0.02) \\ &+ 20S_{\text{U}}(\tilde{c}, 1.02, 0.06)\end{aligned} \tag{A.6}$$

where S_{U} is the step-up function defined as previous.

References

A123 Systems official website (2023), http://www.a123systems.com/.

Ahmed, S., Bloom, I., Jansen, A. N., Tanim, T., Dufek, E. J., Pesaran, A., et al. (2017). Enabling fast charging–A battery technology gap assessment. *Journal of Power Sources*, *367*, 250–262.

Andersson, J. A. E., Gillis, J., Horn, G., Rawlings, J. B., & Diehl, M. (2019). CasADi – A software framework for nonlinear optimization and optimal control. *Mathematical Programming Computation*, *11*(1), 1–36. http://dx.doi.org/10.1007/s12532-018-0139-4.

Anseán, D., Dubarry, M., Devie, A., Liaw, B., García, V., Viera, J., et al. (2016). Fast charging technique for high power $LiFePO_4$ batteries: A mechanistic analysis of aging. *Journal of Power Sources*, *321*, 201–209.

Anseán, D., González, M., Viera, J., García, V., Blanco, C., & Valledor, M. (2013). Fast charging technique for high power lithium iron phosphate batteries: A cycle life analysis. *Journal of Power Sources*, *239*, 9–15.

Bai, P., & Bazant, M. Z. (2014). Charge transfer kinetics at the solid–solid interface in porous electrodes. *Nature Communications*, *5*(1), 1–7.

Bai, P., Cogswell, D. A., & Bazant, M. Z. (2011). Suppression of phase separation in $LiFePO_4$ nanoparticles during battery discharge. *Nano Letters*, *11*(11), 4890–4896.

Baker, D., & Verbrugge, M. (2020). Modeling overcharge at lithiated-graphite porous electrodes plating and dissolution of lithium. *Journal of The Electrochemical Society*, *167*(10), Article 100508.

Bazant, M. Z. (2013). Theory of chemical kinetics and charge transfer based on nonequilibrium thermodynamics. *Accounts of Chemical Research*, *46*(5), 1144–1160.

Berliner, M. D., Cogswell, D. A., Bazant, M. Z., & Braatz, R. D. (2021). Methods—PETLION: Open-source software for millisecond-scale porous electrode theory-based lithium-ion battery simulations. *Journal of The Electrochemical Society*, *168*(9), Article 090504.

Berliner, M. D., Jiang, B., Cogswell, D. A., Bazant, M. Z., & Braatz, R. D. (2022a). Fast charging of lithium-ion batteries by mathematical reformulation as mixed continuous-discrete simulation. In *American control conference* (pp. 5265–5270).

Berliner, M. D., Jiang, B., Cogswell, D. A., Bazant, M. Z., & Braatz, R. D. (2022b). Novel operating modes for the charging of lithium-ion batteries. *Journal of The Electrochemical Society*, *169*(10), Article 100546.

Berliner, M. D., Zhao, H., Das, S., Forsuelo, M., Jiang, B., Chueh, W. H., et al. (2021). Nonlinear identifiability analysis of the porous electrode theory model of lithium-ion batteries. *Journal of The Electrochemical Society*, *168*(9), Article 090546.

Bernardi, D. M., & Go, J.-Y. (2011). Analysis of pulse and relaxation behavior in lithium-ion batteries. *Journal of Power Sources*, *196*(1), 412–427.

Blitzstein, J. K., & Hwang, J. (2015). *Introduction to probability*. Boca Raton, FL: CRC Press.

Bryson, A. E., & Ho, Y.-C. (2018). *Applied optimal control: Optimization, estimation, and control*. Thames, Oxfordshire, England, UK: Routledge.

Caracotsios, M., & Stewart, W. (1995). Sensitivity analysis of initial-boundary-value problems with mixed PDEs and algebraic equations: Applications to chemical and biochemical systems. *Computers & Chemical Engineering*, *19*(9), 1019–1030.

Chaturvedi, N. A., Klein, R., Christensen, J., Ahmed, J., & Kojic, A. (2010). Algorithms for advanced battery-management systems. *IEEE Control Systems Magazine*, *30*(3), 49–68.

Chidsey, C. E. (1991). Free energy and temperature dependence of electron transfer at the metal-electrolyte interface. *Science*, *251*(4996), 919–922.

Dreyer, W., Guhlke, C., & Herrmann, M. (2011). Hysteresis and phase transition in many-particle storage systems. *Continuum Mechanics and Thermodynamics*, *23*, 211–231.

Dreyer, W., Guhlke, C., & Huth, R. (2011). The behavior of a many-particle electrode in a lithium-ion battery. *Physica D: Nonlinear Phenomena*, *240*(12), 1008–1019.

Dreyer, W., Jamnik, J., Guhlke, C., Huth, R., Moškon, J., & Gaberšček, M. (2010). The thermodynamic origin of hysteresis in insertion batteries. *Nature Materials*, *9*(5), 448–453.

Fang, W., Kwon, O. J., & Wang, C.-Y. (2010). Electrochemical–thermal modeling of automotive li-ion batteries and experimental validation using a three-electrode cell. *International Journal of Energy Research*, *34*(2), 107–115.

Ferguson, T. R., & Bazant, M. Z. (2012). Nonequilibrium thermodynamics of porous electrodes. *Journal of The Electrochemical Society*, *159*(12), A1967–A1985.

Ferguson, T. R., & Bazant, M. Z. (2014). Phase transformation dynamics in porous battery electrodes. *Electrochimica Acta*, *146*, 89–97.

Fraggedakis, D., McEldrew, M., Smith, R. B., Krishnan, Y., Zhang, Y., Bai, P., et al. (2021). Theory of coupled ion-electron transfer kinetics. *Electrochimica Acta*, *367*, Article 137432.

Galán, S., Feehery, W. F., & Barton, P. I. (1999). Parametric sensitivity functions for hybrid discrete/continuous systems. *Applied Numerical Mathematics*, *31*(1), 17–47.

Galuppini, G., Berliner, M. D., Cogswell, D. A., Zhuang, D., Bazant, M. Z., & Braatz, R. D. (2023). Nonlinear identifiability analysis of multiphase porous electrode theory-based battery models: A lithium iron phosphate case study. *Journal of Power Sources*, *573*, Article 233009.

Galuppini, G., Berliner, M. D., Lian, H., Zhuang, D., Bazant, M. Z., & Braatz, R. D. (2023). Efficient computation of safe, fast charging protocols for multiphase lithium-ion batteries: A lithium iron phosphate case study. *Journal of Power Sources*, *580*, Article 233272.

Gao, T., Han, Y., Fraggedakis, D., Das, S., Zhou, T., Yeh, C.-N., et al. (2021). Interplay of lithium intercalation and plating on a single graphite particle. *Joule*, *5*(2), 393–414.

Golub, G. H., & Van Loan, C. F. (1996). *Matrix computations*. Baltimore, MD: Johns Hopkins University Press.

Haregewoin, A. M., Wotango, A. S., & Hwang, B.-J. (2016). Electrolyte additives for lithium ion battery electrodes: Progress and perspectives. *Energy & Environmental Science*, *9*(6), 1955–1988.

Hindmarsh, A. C., Brown, P. N., Grant, K. E., Lee, S. L., Serban, R., Shumaker, D. E., et al. (2005). SUNDIALS: Suite of nonlinear and differential/algebraic equation solvers. *ACM Transactions on Mathematical Software*, *31*(3), 363–396.

Hu, X., Li, S., & Peng, H. (2012). A comparative study of equivalent circuit models for Li-ion batteries. *Journal of Power Sources*, *198*, 359–367.

Kollmeyer, P., Hackl, A., & Emadi, A. (2017). Li-ion battery model performance for automotive drive cycles with current pulse and EIS parameterization. In *IEEE transportation electrification conference and expo* (pp. 486–492).

Kolluri, S., Aduru, S. V., Pathak, M., Braatz, R. D., & Subramanian, V. R. (2020). Real-time nonlinear model predictive control (NMPC) strategies using physics-based models for advanced lithium-ion battery management system (BMS). *Journal of The Electrochemical Society*, *167*(6), Article 063505.

Krewer, U., Röder, F., Harinath, E., Braatz, R. D., Bedürftig, B., & Findeisen, R. (2018). Dynamic models of Li-ion batteries for diagnosis and operation: A review and perspective. *Journal of The Electrochemical Society*, *165*(16), A3656–A3673.

Li, Y., El Gabaly, F., Ferguson, T. R., Smith, R. B., Bartelt, N. C., Sugar, J. D., et al. (2014). Current-induced transition from particle-by-particle to concurrent intercalation in phase-separating battery electrodes. *Nature Materials*, *13*(12), 1149–1156.

Luenberger, D. G., & Ye, Y. (1984). *Linear and nonlinear programming*. New York: Springer.

Ma, D. L., Chung, S. H., & Braatz, R. D. (1999). Worst-case performance analysis of optimal batch control trajectories. *AIChE Journal*, *45*(7), 1469–1476.

Marcus, R. A. (1956). On the theory of oxidation-reduction reactions involving electron transfer. I. *The Journal of Chemical Physics*, *24*(5), 966–978.

Marcus, R. (1957). On the theory of oxidation-reduction reactions involving electron transfer. II. Applications to data on the rates of isotopic exchange reactions. *The Journal of Chemical Physics*, *26*(4), 867–871.

Mathieu, R., Briat, O., Gyan, P., & Vinassa, J.-M. (2021). Comparison of the impact of fast charging on the cycle life of three lithium-ion cells under several parameters of charge protocol and temperatures. *Applied Energy*, *283*, Article 116344.

Mohtat, P., Pannala, S., Sulzer, V., Siegel, J. B., & Stefanopoulou, A. G. (2021). An algorithmic safety VEST for Li-ion batteries during fast charging. *IFAC-PapersOnLine*, *54*(20), 522–527.

Mosterman, P. J. (1999). An overview of hybrid simulation phenomena and their support by simulation packages. In *International workshop on hybrid systems: Computation and control* (pp. 165–177).

Nagy, Z. K., & Braatz, R. D. (2004). Open-loop and closed-loop robust optimal control of batch processes using distributional and worst-case analysis. *Journal of Process Control*, *14*(4), 411–422.

Nagy, Z. K., & Braatz, R. D. (2007). Distributional uncertainty analysis using power series and polynomial chaos expansions. *Journal of Process Control*, *17*(3), 229–240.

Nambisan, P., Saha, P., & Khanra, M. (2021). Real-time optimal fast charging of Li-ion batteries with varying temperature and charging behaviour constraints. *Journal of Energy Storage*, *41*, Article 102918.

Nesterov, Y., & Nemirovskii, A. (1994). *Interior-point polynomial algorithms in convex programming*. Philadelphia, Pennsylvania, United States: SIAM.

Newman, J. (1998). FORTRAN programs for simulation of electrochemical systems: Dualfoil, University of California, Berkeley. http://www.cchem.berkeley.edu/jsngrp/fortran.html.

Newman, J., & Thomas-Alyea, K. E. (2012). *Electrochemical systems*. Hoboken, New Jersey: John Wiley & Sons.

Newman, J., & Tiedemann, W. (1975). Porous-electrode theory with battery applications. *AIChE Journal*, *21*(1), 25–41.

Nikolić, D. D. (2016). DAE tools: Equation-based object-oriented modelling, simulation and optimisation software. *PeerJ Computer Science*, *2*, Article e54.

Notten, P. H., Bert, O. h. V., & Van Beek, J. (2005). Boostcharging Li-ion batteries: A challenging new charging concept. *Journal of Power Sources*, *145*(1), 89–94.

Pedret Sagnier, B. (2022). *Stochastic optimal control of lithium-ion battery operations* [B.S. thesis], Universitat Politècnica de Catalunya, Barcelona, Spain.

Pei, A., Zheng, G., Shi, F., Li, Y., & Cui, Y. (2017). Nanoscale nucleation and growth of electrodeposited lithium metal. *Nano Letters*, *17*(2), 1132–1139.

Perez, H., Dey, S., Hu, X., & Moura, S. (2017). Optimal charging of Li-ion batteries via a single particle model with electrolyte and thermal dynamics. *Journal of The Electrochemical Society*, *164*(7), A1679–A1687.

Persson, K., Hinuma, Y., Meng, Y. S., Van der Ven, A., & Ceder, G. (2010). Thermodynamic and kinetic properties of the Li-graphite system from first-principles calculations. *Physical Review B*, *82*(12), Article 125416.

Pozzi, A., Moura, S., & Toti, D. (2023). A deep learning-based predictive controller for the optimal charging of a lithium-ion cell with non-measurable states. *Computers & Chemical Engineering*, *173*, Article 108222.

Pozzi, A., & Raimondo, D. M. (2022). Stochastic model predictive control for optimal charging of electric vehicles battery packs. *Journal of Energy Storage*, *55*, Article 105332.

Pozzi, A., Torchio, M., Braatz, R. D., & Raimondo, D. M. (2020). Optimal charging of an electric vehicle battery pack: A real-time sensitivity-based model predictive control approach. *Journal of Power Sources*, *461*, Article 228133.

Pozzi, A., & Toti, D. (2022). Lexicographic model predictive control strategy in ageing-aware optimal charging procedure for lithium-ion batteries. *Computers & Chemical Engineering*, *163*, Article 107847.

Rawlings, J. B., Mayne, D. Q., & Diehl, M. (2017). *Model predictive control: Theory, computation, and design* (2nd ed.). Madison, WI: Nob Hill Publishing.

Schlegel, M., Stockmann, K., Binder, T., & Marquardt, W. (2005). Dynamic optimization using adaptive control vector parameterization. *Computers & Chemical Engineering*, *29*(8), 1731–1751.

Severson, K. A., Attia, P. M., Jin, N., Perkins, N., Jiang, B., Yang, Z., et al. (2019). Data-driven prediction of battery cycle life before capacity degradation. *Nature Energy*, *4*(5), 383–391.

Smith, R. B., & Bazant, M. Z. (2017). Multiphase porous electrode theory. *Journal of The Electrochemical Society*, *164*(11), E3291–E3310.

Speltino, C., Di Domenico, D., Fiengo, G., & Stefanopoulou, A. (2009). Comparison of reduced order lithium-ion battery models for control applications. In *Proceedings of the 48h IEEE conference on decision and control held jointly with 28th Chinese control conference* (pp. 3276–3281).

Srinivasan, B., Palanki, S., & Bonvin, D. (2003). Dynamic optimization of batch processes: I. Characterization of the nominal solution. *Computers & Chemical Engineering*, *27*(1), 1–26.

Tarascon, J., & Armand, M. (2011). Issues and challenges facing rechargeable lithium batteries. *Nature*, *414*(6861), 359–367.

Tomaszewska, A., Chu, Z., Feng, X., O'Kane, S., Liu, X., Chen, J., et al. (2019). Lithium-ion battery fast charging: A review. *ETransportation*, *1*, Article 100011.

Torchio, M., Magni, L., Gopaluni, R. B., Braatz, R. D., & Raimondo, D. M. (2016). LIONSIMBA: A Matlab framework based on a finite volume model suitable for Li-ion battery design, simulation, and control. *Journal of The Electrochemical Society*, *163*(7), A1192–A1205.

Valøen, L. O., & Reimers, J. N. (2005). Transport properties of $LiPF_6$-based Li-ion battery electrolytes. *Journal of The Electrochemical Society*, *152*(5), A882–A891.

Xu, M., Wang, R., Reichman, B., & Wang, X. (2018). Modeling the effect of two-stage fast charging protocol on thermal behavior and charging energy efficiency of lithium-ion batteries. *Journal of Energy Storage*, *20*, 298–309.

Xu, M., Wang, X., Zhang, L., & Zhao, P. (2021). Comparison of the effect of linear and two-step fast charging protocols on degradation of lithium-ion batteries. *Energy*, *227*, Article 120417.

Xu, M., Wang, R., Zhao, P., & Wang, X. (2019). Fast charging optimization for lithium-ion batteries based on dynamic programming algorithm and electrochemical-thermal-capacity fade coupled model. *Journal of Power Sources*, *438*, Article 227015.

Zou, C., Manzie, C., & Anwar, S. (2014). Control-oriented modeling of a lithium-ion battery for fast charging. *IFAC Proceedings Volumes*, *47*(3), 3912–3917.

Zou, C., Manzie, C., & Nešić, D. (2018). Model predictive control for lithium-ion battery optimal charging. *IEEE/ASME Transactions on Mechatronics*, *23*(2), 947–957.